

High-resolution Fourier-transform infrared chemical imaging with multiple synchrotron beams

Michael J Nasse^{1,2}, Michael J Walsh³, Eric C Mattson¹, Ruben Reininger⁴, André Kajdacsy-Balla⁵, Virgilia Macias⁵, Rohit Bhargava³ & Carol J Hirschmugl¹

Conventional Fourier-transform infrared (FTIR) microspectroscopic systems are limited by an inevitable trade-off between spatial resolution, acquisition time, signal-to-noise ratio (SNR) and sample coverage. We present an FTIR imaging approach that substantially extends current capabilities by combining multiple synchrotron beams with wide-field detection. This advance allows truly diffraction-limited high-resolution imaging over the entire mid-infrared spectrum with high chemical sensitivity and fast acquisition speed while maintaining high-quality SNR.

Stains and labels to enhance contrast in microscopy have been used for many years, leading to many important discoveries. However, their use is often time-consuming and cumbersome, can perturb the function of drugs or small metabolites or may be cytotoxic. In contrast, label-free chemical imaging requires no artificial modification of biomolecules or additional sample preparation and permits a comprehensive characterization of heterogeneous materials¹. Chemical imaging is generating considerable interest for biomedical analysis as dyes or stains are not required for contrast and substantial chemical and structural information can be extracted without prior knowledge of molecular epitopes or manual interpretation. Vibrational spectroscopic techniques, including both mid-infrared absorption and Raman scattering-based imaging, permit molecular analyses without perturbation. Spontaneous Raman scattering relies on a very weak effect and therefore involves a trade-off between measurement time and sensitivity, potentially leading to photoinduced sample damage. Emerging instrumentation² involving nonlinear Raman contrast has considerably extended imaging capabilities beyond these traditional trade-offs, and exciting work is underway to carefully match lasers and reject spurious backgrounds (for example, in coherent anti-Stokes Raman scattering) and in extending wavelength

coverage and speed (for example, in stimulated Raman scattering). Conversely, the strong mid-infrared absorption contrast makes infrared spectroscopy and microscopy a straightforward, non-destructive, label-free chemical contrast modality with broad applications^{1,3} ranging from the analysis of graphene-based materials, pharmaceuticals, volcanic rocks and biominerals to applications in forensics and art conservation, among others. Infrared spectroscopic tools are particularly interesting for applications in biomedical fields such as marine biology, cancer research, stem cells (for example, to delineate cell mechanisms or lineage), real-time monitoring of live cells, Alzheimer's disease, Malaria parasites and more³ (Online Methods).

Infrared instrumentation, however, has stagnated mostly owing to spectral-spatial trade-offs. Commonly, low-brightness thermal sources and synchrotron sources are used for Fourier-transform infrared (FTIR) microspectroscopy. Synchrotron sources yield stable, broadband and high-brightness radiation, making them excellent for FTIR microspectroscopy, but the flux of conventional single-beam beamlines is limited by the relatively small horizontal collection angle and the resulting comparatively small source étendue makes them challenging to use with wide-field imaging characterized by a relatively large acceptance or étendue (**Supplementary Note 1**). Here we used multiple synchrotron beams with a wide-field detection scheme. This allowed us to acquire truly diffraction-limited, high-spatial-resolution infrared images of high spectral quality with outstanding speed, considerably extending the potential of infrared microscopy.

For an optical system permitting diffraction-limited imaging, spatial resolution is defined as the capacity to separate two adjacent (point-like) objects. To achieve the highest (diffraction-limited) resolution, an objective with the largest possible numerical aperture (NA) should be used, and the instrument's signal-to-noise ratio (SNR)^{4,5} should be optimized. Also, it is indispensable to match the image pixilation to the NA of the objective using the appropriate spatial sampling or pixel size. Too-large pixels inevitably lead to resolution loss, whereas smaller pixels do not improve the resolution further. A detailed analysis⁴ (Online Methods) shows that, assuming the largest commercially available NA of ~0.65, diffraction-limited resolution over the entire mid-infrared spectrum can only be achieved with an effective pixel spacing not larger than $\sim\lambda/4$ or $\sim 0.6\ \mu\text{m}$ for the shortest wavelength of interest ($\lambda = 2.5\ \mu\text{m}$).

One approach to infrared microscopy uses a single element detector and confocal-like apertures to localize light incident on the sample. In this configuration, pixel size is given by the raster-scanning step size⁴. Apertures of dimension a only deliver

¹Department of Physics, University of Wisconsin-Milwaukee, Milwaukee, Wisconsin, USA. ²Synchrotron Radiation Center, University of Wisconsin-Madison, Stoughton, Wisconsin, USA. ³Department of Bioengineering, Micro and Nanotechnology Laboratory and Beckman Institute for Advanced Science and Technology, University of Illinois at Urbana-Champaign, Urbana, Illinois, USA. ⁴Scientific Answers and Solutions, Mount Sinai, New York, USA. ⁵Department of Pathology, University of Illinois at Chicago, Chicago, Illinois, USA. Correspondence should be addressed to R.B. (rxb@illinois.edu) or C.J.H. (cjhirsch@uwm.edu).

RECEIVED 18 OCTOBER 2010; ACCEPTED 22 FEBRUARY 2011; PUBLISHED ONLINE 20 MARCH 2011; DOI:10.1038/NMETH.1585

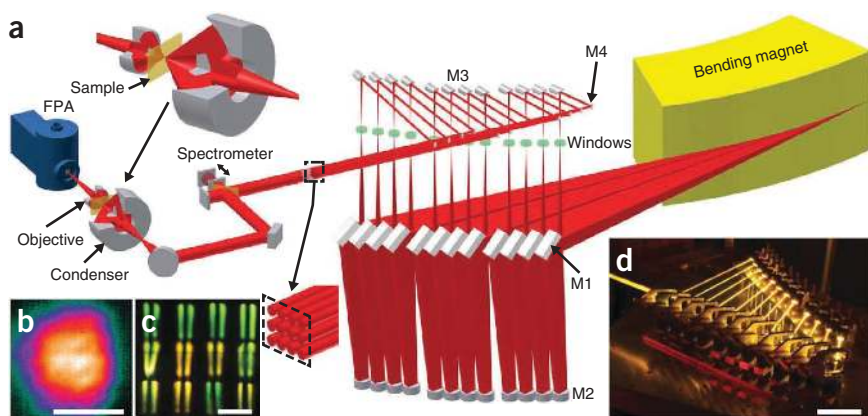


Figure 1 | FTIR imaging with a multibeam synchrotron source. (a) Schematic of the experimental setup. M1–M4 are mirror sets. (b) A full 128×128 pixel FPA image with 12 overlapping beams illuminating an area of $\sim 50 \mu\text{m} \times 50 \mu\text{m}$. Scale bar, $40 \mu\text{m}$. (c) A visible-light photograph of the 12 beams projected on a screen in the beam path (dashed box in a). Scale bar, $\sim 1.5 \text{ cm}$. We display the beams as one beam from then on in the schematics. Each beam exhibits a shadow cast by a cooling tube upstream, which is not shown in a. (d) Long-exposure photograph showing the combination of the 12 individual beams into the beam bundle by mirrors M3 and M4. Scale bar, $\sim 20 \text{ cm}$.

diffraction-limited resolution⁶ when $\lambda \geq a$. For $\lambda < a$, diffraction-limited resolution⁶ is not attained, whereas for longer wavelengths the throughput decays rapidly. This trade-off between resolution and throughput (or SNR) is particularly penalizing for infrared microspectroscopy because of the broad bandwidth. In practice, reasonable SNR limits the smallest aperture for the illumination at the sample plane to $\sim 10 \mu\text{m} \times 10 \mu\text{m}$ for a thermal source⁶ and, in a few demonstrations⁷, down to $\sim 3 \mu\text{m} \times 3 \mu\text{m}$ for synchrotron sources. The small aperture transmissivity

of only a few percent makes point-by-point sampling systems very inefficient because of the dual need for signal averaging to obtain high SNR and rastering a small pixel size to acquire data, leading to exceedingly long acquisition times. These trade-offs make sequential point sampling impractical for micrometer-scale aperture sizes and sub-micrometer-scale raster step sizes (necessary for correct spatial sampling⁴) to achieve diffraction-limited maps. For example, it takes 2–4 h to acquire an area of only $30 \mu\text{m} \times 30 \mu\text{m}$ as a fully diffraction-limited map at a state-of-the-art third-generation synchrotron⁷ equipped with a conventional confocal system. Lengthy collection times, in most practical cases, lead experimenters to choose larger aperture and step sizes, thereby compromising the achievable spatial resolution. In contrast, our system can cover this area in under a minute without compromising the spatial sampling required for diffraction-limited resolution.

We based our approach on the more recent strategy of wide-field imaging using multichannel focal plane array (FPA) detectors^{8–10}, in which no lossy apertures are used. This increases spatial coverage and imaging speed greatly, but the SNR using a thermal source limits pixel sizes to $\sim 5 \mu\text{m} \times 5 \mu\text{m}$ at the sample plane. Achieving a pixel size ~ 100 times smaller to correctly sample the diffraction-limited illumination is very ineffective, resulting in a

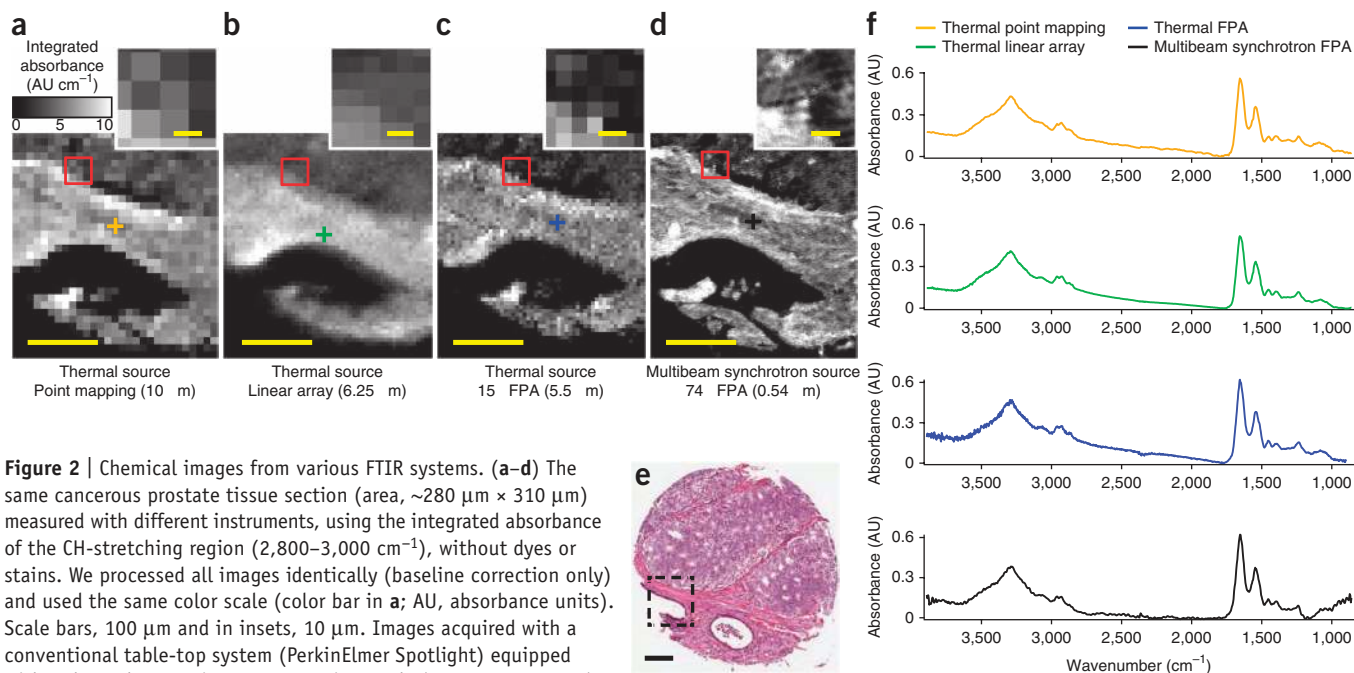


Figure 2 | Chemical images from various FTIR systems. (a–d) The same cancerous prostate tissue section (area, $\sim 280 \mu\text{m} \times 310 \mu\text{m}$) measured with different instruments, using the integrated absorbance of the CH-stretching region ($2,800\text{--}3,000 \text{ cm}^{-1}$), without dyes or stains. We processed all images identically (baseline correction only) and used the same color scale (color bar in a; AU, absorbance units). Scale bars, $100 \mu\text{m}$ and in insets, $10 \mu\text{m}$. Images acquired with a conventional table-top system (PerkinElmer Spotlight) equipped with a thermal source in raster-scanning mode ($10 \mu\text{m} \times 10 \mu\text{m}$; a) and linear array mode ($6.25 \mu\text{m} \times 6.25 \mu\text{m}$; b), with an FTIR imaging system (Varian Stingray) equipped with a $64 \text{ pixel} \times 64 \text{ pixel}$ FPA ($5.5 \times 5.5 \mu\text{m}$ per pixel at the sample plane; c) and with our multibeam synchrotron-based imaging system (pixel size, $0.54 \mu\text{m} \times 0.54 \mu\text{m}$; d). (e) Hematoxylin and eosin (H&E)-stained prostate tissue (diameter, 0.75 mm). Scale bar, $100 \mu\text{m}$. Dashed box specifies the corresponding area of a serial, unstained section from which we generated images in a–d. (f) Typical unprocessed spectra from a single pixel acquired with each instrument (crosshairs in a–d indicate corresponding pixel positions in the infrared images).

~ 100 -fold lower SNR (**Supplementary Fig. 1**) and thus in a $\sim 10^4$ -fold longer scanning time⁸. Hence, to our knowledge there are no reports of a true diffraction-limited FTIR imaging system with a thermal source.

In 2006 independent groups^{11–13} pioneered the coupling of a synchrotron beam with an FPA detector, which is not obvious because wide-field illumination seems incompatible with a small, low-emittance synchrotron beam. These groups demonstrated that, with a single synchrotron beam, a local region of the FPA can be illuminated, and that this region yielded increased SNR compared to thermal sources. This inhomogeneous illumination, however, means that either a relatively small FPA (and thus sample area) must be used or that the acquisition time must be increased to compensate the inhomogeneous illumination. This coverage-SNR trade-off has hampered the use of synchrotron-based technology: only one recent publication¹⁴ uses a single synchrotron beam with an FPA.

Here we present an infrared imaging system specifically designed and optimized to overcome these limitations by coupling

multiple low-emittance synchrotron beams with a large FPA detector. We extracted a large fan of radiation from a dedicated bending magnet, split it into 12 beams and subsequently rearranged these into a 3×4 matrix beam bundle to illuminate a large field of view in the sample plane (**Fig. 1**). We engineered the matrix to achieve homogeneous illumination over areas of up to $52 \mu\text{m} \times 52 \mu\text{m}$ ($96 \text{ pixels} \times 96 \text{ pixels}$; **Fig. 1b** and **Supplementary Fig. 2**) with each pixel corresponding to $0.54 \mu\text{m} \times 0.54 \mu\text{m}$ at the sample plane. This pixel size, ~ 100 times smaller than conventional thermal or synchrotron systems, is smaller than the maximum pixel size allowed for correct spatial sampling (oversampling) so that diffraction-limited images even at the smallest wavelength of interest ($2.5 \mu\text{m}$) are possible (Online Methods). Although we designed this system explicitly for acquisition in transmission mode, it also yields equivalent quality images in reflection mode (**Supplementary Figs. 3 and 4**).

To test this approach, we compared data from the same prostate tissue using various state-of-the-art infrared imaging systems

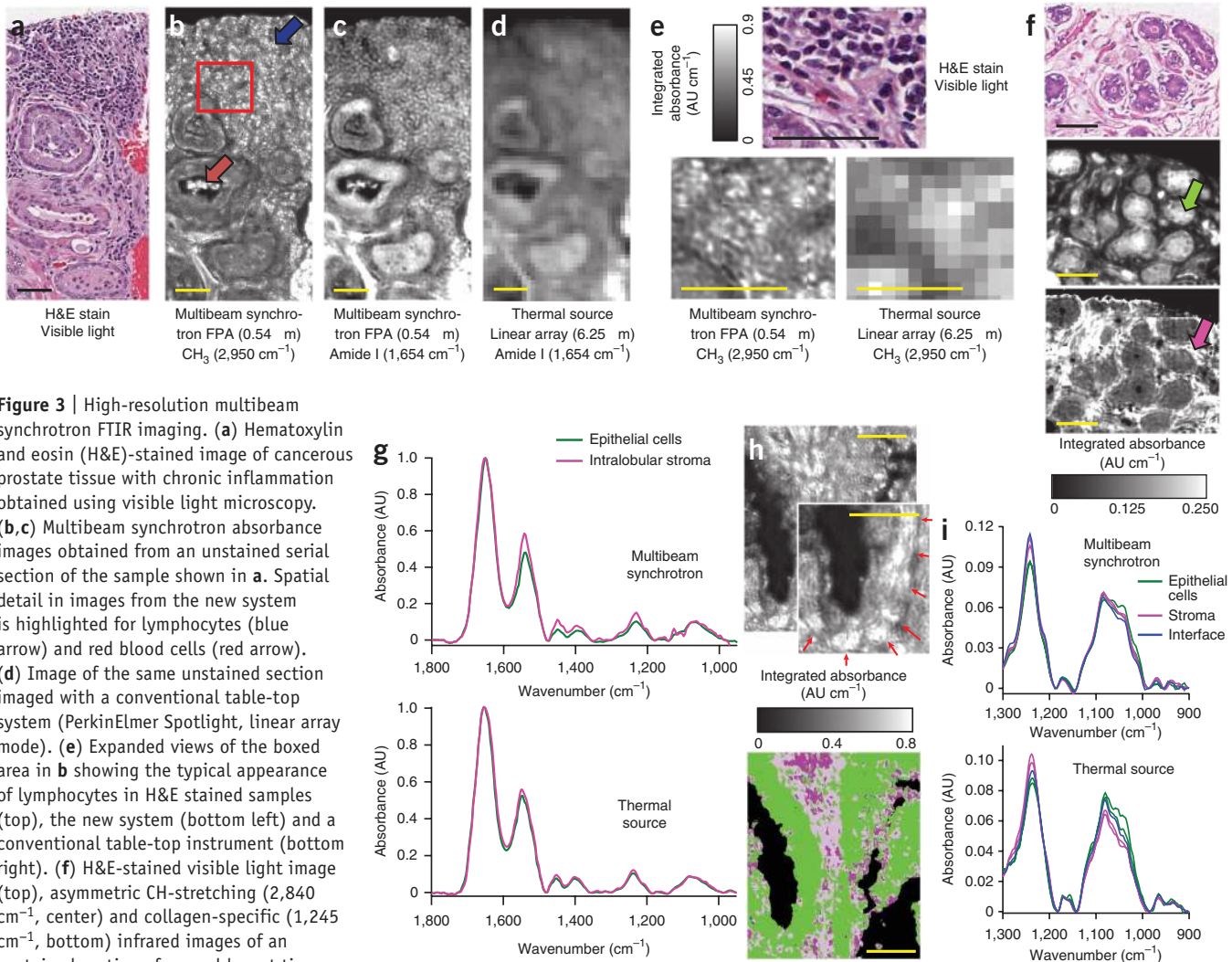


(Fig. 2 and Supplementary Fig. 1). None of the other instruments provided diffraction-limited resolution at all wavelengths (Fig. 2a–c). Raster-scanning the area shown in Figure 2a–d (~280 μm \times 310 μm) at diffraction-limited resolution using a synchrotron-based dual-aperture microscope would require over 11 d. In contrast, using our technique we recorded the same area (Fig. 2d) in ~30 min (16 scans). The spectral quality was essentially identical (Fig. 2f) to that of the best commercial systems, despite the ~100-fold pixel area reduction. This pixel size provided the additional spatial detail (Fig. 2) necessary for infrared imaging to become competitive with optical microscopy in biomedical applications. In another example, wide-field multibeam synchrotron imaging revealed lymphocytes (diameter, ~2–7 μm) and other tissue features that were clearly visible in hematoxylin and eosin–stained images (the clinical gold standard for diagnosis; Fig. 3a–c). The same visualizations were impossible using conventional table-top infrared systems (Fig. 3d,e). The contrast in these images can be used to color-code images into constituent cell types¹⁵; hence the capability of our technique opens up the possibility of subcellular classification.

Furthermore, pixel localization also improved spectral purity of data extracted from images. The hematoxylin and eosin contrast was well-reproduced with our technique using simple absorption features, and epithelial and stromal regions were clearly delineated without staining (Fig. 3f). The additional detail in synchrotron wide-field images allowed relatively limited cross-contamination of spectra from both intralobular stromal and epithelial regions. Although we expected these characteristic spectra to be different, the limited pixel size of the thermal source systems demonstrated substantial overlap, but the multibeam synchrotron system provided distinct spectra (Fig. 3g). Using our technique, we also classified an infrared image of prostate tissue into constituent cell types (Fig. 3h). Although it is well-known that the basement membrane lies at the interface of epithelial and stromal cells and is critical in diagnosing lethal cancer, the basement membrane is not discernable in images from thermal systems. We classified infrared tissue images into cell types¹⁵, and identified the interface between the epithelial and stromal cells (Fig. 3h). Thermal source spectra from these regions were an average of epithelial and stromal pixels, whereas interface spectra extracted from the synchrotron image were distinct from both contributions (Fig. 3i), which, with the higher collagen triplet absorption, was suggestive of the basement membrane. Additional investigations are in progress.

To validate the optical capability of our system, we recorded images of a 1951 US Air Force test target⁵ (Supplementary Figs. 3a,b and 4). We used line profiles⁵ (Supplementary Fig. 3e–h) to determine the contrast for each pattern, quantitatively confirming that our system reached and exceeded (Supplementary Note 2) the Rayleigh resolution criterion and delivered diffraction-limited images over the entire mid-infrared bandwidth. Furthermore, spatial oversampling at all wavelengths and high SNR, as offered by our system, are a prerequisite^{12,13} for developing computational resolution enhancement techniques. We implemented a spatial deconvolution algorithm (Supplementary Note 3) based on (wavelength-dependent) measured point-spread functions (Supplementary Figs. 5 and 6). The increased contrast and resolution of the deconvolved US Air Force target sample images were apparent in the line profiles (Supplementary Fig. 3c–h). Furthermore, measurements of ~1 μm polystyrene

beads confirmed that our system reached a spectral limit of detection of 6 ± 1 fmol (mass, 600 ± 100 fg; and volume, 0.6 ± 0.1 fl) in a single $0.54 \mu\text{m} \times 0.54 \mu\text{m}$ pixel (Supplementary Fig. 7). We estimated that this limit is about two orders of magnitude finer than that of present instrumentation¹⁶.

The use of multiple synchrotron beams enabled us to achieve a homogeneously high SNR over a large FPA area, which improved sample coverage and acquisition speed compared to conventional thermal or synchrotron-based systems and enabled high diffraction-limited spatial resolution over the entire mid-infrared spectrum. The improvement in acquisition time opens the way to real-time noninvasive and label-free live-cell imaging. We hope that our technique spurs the community to develop appropriate optical designs for tabletop instruments and provides a rationale for laser-based systems and other multibeam synchrotron-based imaging beamlines.

METHODS

Methods and any associated references are available in the online version of the paper at <http://www.nature.com/naturemethods/>.

Note: Supplementary information is available on the Nature Methods website.

ACKNOWLEDGMENTS

We thank T. Kubala, S. Janowski and M. Fisher for their engineering work, and Z. El-Bayyari for his help during alignment of the beamline. This work was supported by the US National Science Foundation under awards CHE-0832298, CHE-0957849 and DMR-0619759, and by the Research Growth Initiative of the University of Wisconsin–Milwaukee. Part of this work is based on research conducted at the Synchrotron Radiation Center, University of Wisconsin–Madison, which is supported by the National Science Foundation under award DMR-0537588. The project described was also supported by award R01CA138882 from the US National Institutes of Health.

AUTHOR CONTRIBUTIONS

M.J.N., R.R. and C.J.H. designed research; M.J.N., M.J.W. and E.C.M. performed research; M.J.W., A.K.-B., V.M. and R.B. contributed prostate samples; M.J.N., M.J.W., E.C.M., R.B. and C.J.H. analyzed data; and M.J.N., R.B. and C.J.H. wrote the paper.

COMPETING FINANCIAL INTERESTS

The authors declare competing financial interests: details accompany the full-text HTML version of the paper at <http://www.nature.com/naturemethods/>.

Published online at <http://www.nature.com/naturemethods/>.

Reprints and permissions information is available online at <http://npg.nature.com/reprintsandpermissions/>.

- Wetzel, D.L. & LeVine, S.M. *Science* **285**, 1224–1225 (1999).
- Pezacki, J.P. *et al. Nat. Chem. Biol.* **7**, 137–145 (2011).
- Chalmers, J.M. & Griffiths, P.R. *Handbook of Vibrational Spectroscopy* (Wiley, 2002).
- Stelzer, E.H.K. *J. Microsc.* **189**, 15–24 (1998).
- Lasch, P. & Naumann, D. *Biochim. Biophys. Acta* **1758**, 814–829 (2006).
- Carr, G.L. *Rev. Sci. Instrum.* **72**, 1613–1619 (2001).
- Dumas, P., Jamin, N., Teillaud, J.L., Miller, L.M. & Beccard, B. *Faraday Discuss.* **126**, 289–302 (2004).
- Bhargava, R. & Levin, I.W. *Anal. Chem.* **73**, 5157–5167 (2001).
- Lewis, E.N. *et al. Anal. Chem.* **67**, 3377–3381 (1995).
- Kidder, L.H., Levin, I.W., Lewis, E.N., Kleiman, V.D. & Heilweil, E.J. *Opt. Lett.* **22**, 742–744 (1997).
- Moss, D., Gasharova, B. & Mathis, Y. *Infrared Phys. Technol.* **49**, 53–56 (2006).
- Carr, G.L., Chubar, O. & Dumas, P. in *Spectrochemical Analysis Using Infrared Multichannel Detectors* 1st edn. (eds., Bhargava, R. & Levin, I.W.) 56–84 (Wiley-Blackwell, Oxford, 2005).
- Miller, L.M. & Dumas, P. *Biochim. Biophys. Acta* **1758**, 846–857 (2006).
- Petibois, C., Cestelli-Guidi, M., Piccinini, M., Moenner, M. & Marcelli, A. *Anal. Bioanal. Chem.* **397**, 2123–2129 (2010).
- Fernandez, D.C., Bhargava, R., Hewitt, S.M. & Levin, I.W. *Nat. Biotechnol.* **23**, 469–474 (2005).
- Bhargava, R., Schwartz Perlman, R., Fernandez, D.C., Levin, I.W. & Bartick, E.G. *Anal. Bioanal. Chem.* **394**, 2069–2075 (2009).

ONLINE METHODS

Requirements for diffraction-limited resolution. Mid-infrared spectroscopy and microscopy has very broad applications in many scientific fields, ranging from fundamental and applied research to engineering and biology^{15–29}. Infrared microspectroscopy in particular can contribute to the biomedical sciences because of its noninvasive spatially resolved chemical specificity. Here we describe the requirements to obtain diffraction-limited spatial resolution with a mid-infrared microscope.

Spatial resolution can be quantified, for example, by the Rayleigh⁵ criterion as $d = 0.61 \lambda / \text{NA}$, in which d is the minimum distance between two adjacent (point-like) objects that are just resolved (the factor 0.61 is strictly valid only for lenses without obscuration and smaller for Schwarzschild optics; see **Supplementary Note 2**). But achievable spatial resolution is not only dependent on the wavelength and the NA of the objective via the Rayleigh criterion but also on the pixel size, that is, the objective's magnification and the SNR of the imaging system⁴. To observe diffraction-limited performance, a spatial sampling of at least ~ 8 pixels⁴ per Airy pattern is required to achieve sufficient contrast. Smaller pixel sizes (oversampling) do not improve the resolution, which is then limited by diffraction, whereas larger pixels unavoidably deteriorate contrast and thus resolution (undersampling). For the smallest wavelength ($2.5 \mu\text{m}$) using an NA of 0.65, we need a pixel size not larger than $1.22 \times 2.5 \mu\text{m} / 0.65 / 8 = 0.59 \mu\text{m}$. Even the less restrictive Nyquist theorem yields a maximum pixel size of $1 / (2.3 f_{\text{cutoff}}) = 0.84 \mu\text{m}$ (usually 2.3 is used instead of the theoretical 2 suggested by Nyquist to account for factors such as noise in real optical systems³⁰), where $f_{\text{cutoff}} = 2 \text{NA} / \lambda$ is the spatial cutoff frequency, equivalent to the Sparrow frequency^{5,31}. In summary, this means that the NA of an objective alone is not enough to provide the resolution promised by the Rayleigh criterion, but its magnification also has to match. In the case of an objective with an NA of 0.65 (approximately the largest commercially available NA, giving the best possible spatial resolution), it needs at least a magnification of $40 \mu\text{m} / 0.59 \mu\text{m} = 68$ (assuming a typical FPA pixel size of $40 \mu\text{m} \times 40 \mu\text{m}$). We used a $74\times$ objective (NA = 0.65) in our setup, leading to a pixel size of $0.54 \mu\text{m} \times 0.54 \mu\text{m}$ (slight oversampling). In addition this high spatial sampling offers the advantage that subdiffraction objects can be localized (but of course, not resolved) with an accuracy better than the diffraction limit³².

Instrument design. Synchrotron storage rings are excellent light sources for aperture-based infrared microspectroscopy³³ as the small horizontal and vertical emittance (source étendue) of conventional single-beam beamlines and the relatively small acceptance (detector system étendue) of the microscopy system can be closely matched (**Supplementary Table 1**). Increasing the photon flux by extracting a larger horizontal angle from a bending magnet, however, is not beneficial because the additional photons cannot be coupled efficiently to the small acceptance of such microscopy systems. For wide-field microscopes without throughput-restricting apertures, in contrast, single beams from conventional beamlines have limited flux owing to their relatively small emittance, making it challenging to match the relatively large acceptance of a multichannel FPA imaging instrument. The instrument described here substantially increased the horizontal collection angle to match the large acceptance of a

wide-field imaging system to fully exploit the source brightness. It is located at the Synchrotron Radiation Center in Stoughton, Wisconsin, USA, which already houses a conventional aperture-based infrared microscope. This synchrotron facility encourages scientists to apply for peer-reviewed access to beamtime and/or initiate a collaboration with the authors of this work. Applications are accepted for review every six months and rapid requests for initial experiments are handled more frequently (http://www.src.wisc.edu/users/new_users.html).

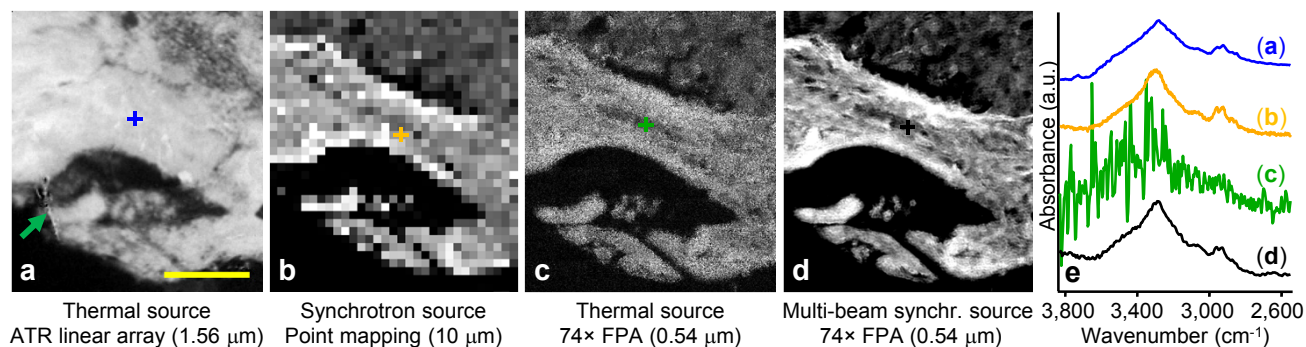
We extracted $320 \text{ mrad} \times 27 \text{ mrad}$ of infrared radiation from a dedicated bending magnet and split this fan of radiation into twelve beams with a set of twelve toroidal mirrors (M1; **Fig. 1**), which refocused each beam (magnification of 1). Each beam exited an ultrahigh vacuum chamber via one of twelve flat mirrors (M2; **Fig. 1**) through one of twelve ZnSe windows (**Fig. 1**) into a nitrogen-purged area. Next, twelve parabolic mirrors (M3; **Fig. 1**) collimated the beams, followed by twelve stacked small flat mirrors (M4; **Fig. 1**) that rearranged the beams into a 3×4 matrix. We used a subsequent piezo-driven optical feedback system (feedback system is not shown) to stabilize the beam bundle, reduce vibration effects and increase the SNR. Next, we sent the bundle through a Vertex 70 (Bruker) spectrometer (**Fig. 1**), which was coupled to a Hyperion 3000 (Bruker) infrared and visible light microscope. There, the slightly defocused beam bundle illuminated the sample area through a $15\times$ or $20\times$ Schwarzschild condenser (**Fig. 1**) to spread out each beam so that the beams overlap spatially to provide quasi-homogeneous illumination at the sample. Finally, a $74\times$ objective (Ealing) imaged the sample onto a $128 \text{ pixel} \times 128 \text{ pixel}$ FPA (Santa Barbara Focalplane), so that each pixel had an effective geometrical area at the sample plane of $0.54 \mu\text{m} \times 0.54 \mu\text{m}$ (**Fig. 1**). Additional design details of the imaging system have been reported elsewhere³⁴. In contrast to other implementations of thermal or synchrotron sources, our multibeam system allowed us to simultaneously uniformly illuminate an order of magnitude more pixels ($96 \text{ pixels} \times 96 \text{ pixels}$; **Fig. 1b**) and used an objective with a substantially higher NA of 0.65 with a correctly matched⁴ pixel size ($0.54 \mu\text{m} \times 0.54 \mu\text{m}$) to maintain full high diffraction-limited resolution over the mid-infrared spectrum at a high SNR. We used a condenser with an NA of ~ 0.6 to match the NA of the objective. Owing to its higher NA, this objective delivered 38% and 23% higher spatial resolution (according to the Rayleigh criterion) compared to previous studies (for example, the $15\times$ objective with NA = 0.4 and pixel size = $2.7 \mu\text{m} \times 2.7 \mu\text{m}$ or $36\times$ objective with NA = 0.5 and pixel size = $1.1 \mu\text{m} \times 1.1 \mu\text{m}$)^{11,14}. Furthermore, owing to the multibeam design, a high synchrotron storage ring current was not mandatory to obtain high SNR. The $\sim 270 \text{ mA}$ current of our storage ring was sufficient to achieve similar SNR (**Fig. 2d,f**) leading to shorter acquisition times compared to those reported in previous publications¹⁴. The present design can cover more than double the sample area in equivalent or shorter times with better spatial resolution as compared to single synchrotron beam systems.

Synchrotron sources may have coherent properties, for example, synchrotrons with pulse lengths shorter than tens of femtoseconds in the far infrared. The present source, however, had nanosecond pulses, and we designed the path lengths for the twelve beams to never temporally overlap on the sample or detector plane. Hence, temporal coherence did not have an impact on the imaging quality of the images produced by the microscope. Experimentally we

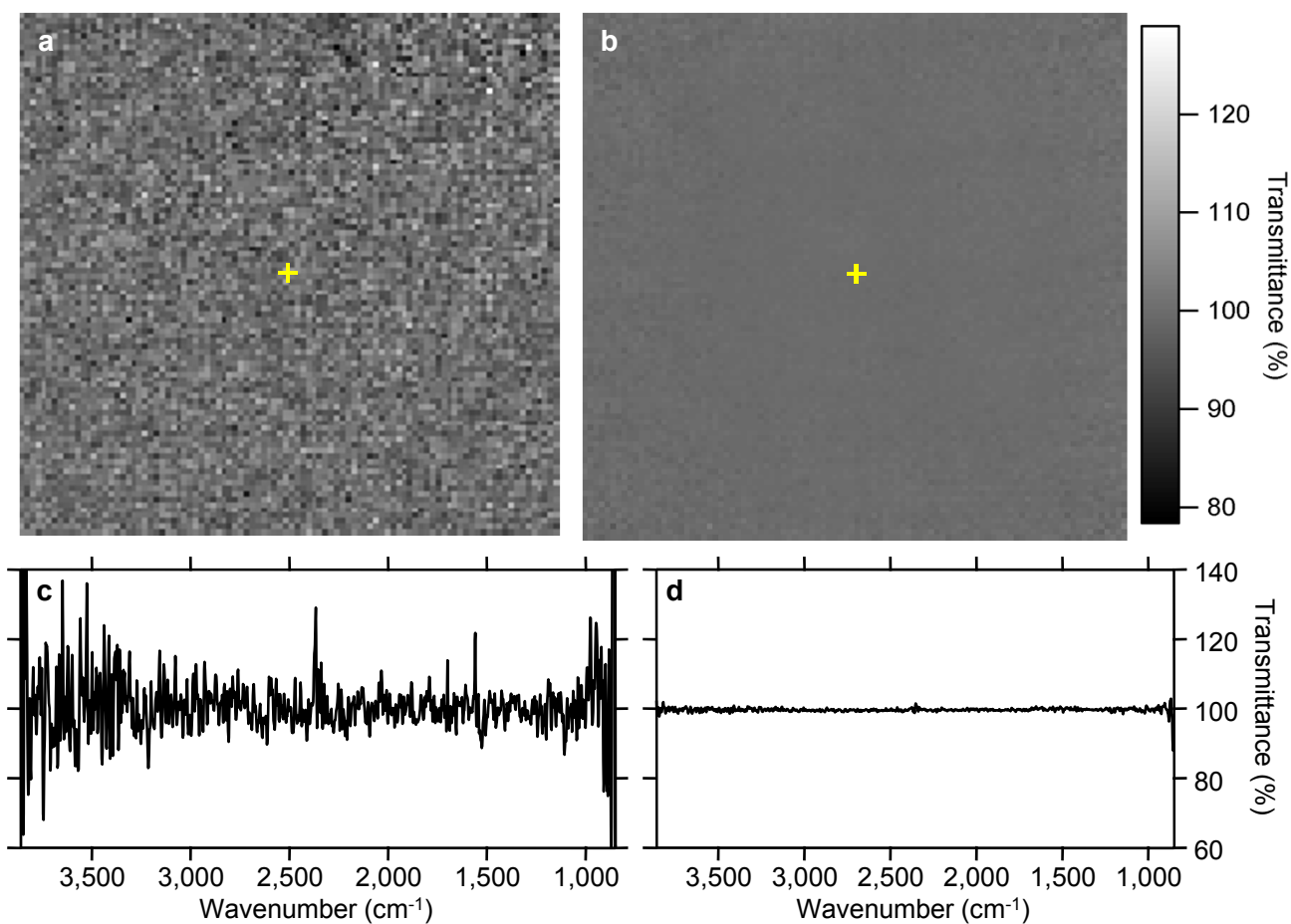
High-resolution Fourier-transform infrared chemical imaging with multiple synchrotron beams

Michael J Nasse, Michael J Walsh, Eric C Mattson, Ruben Reininger, André Kajdacsy-Balla, Virgilia Macias, Rohit Bhargava & Carol J Hirschmugl

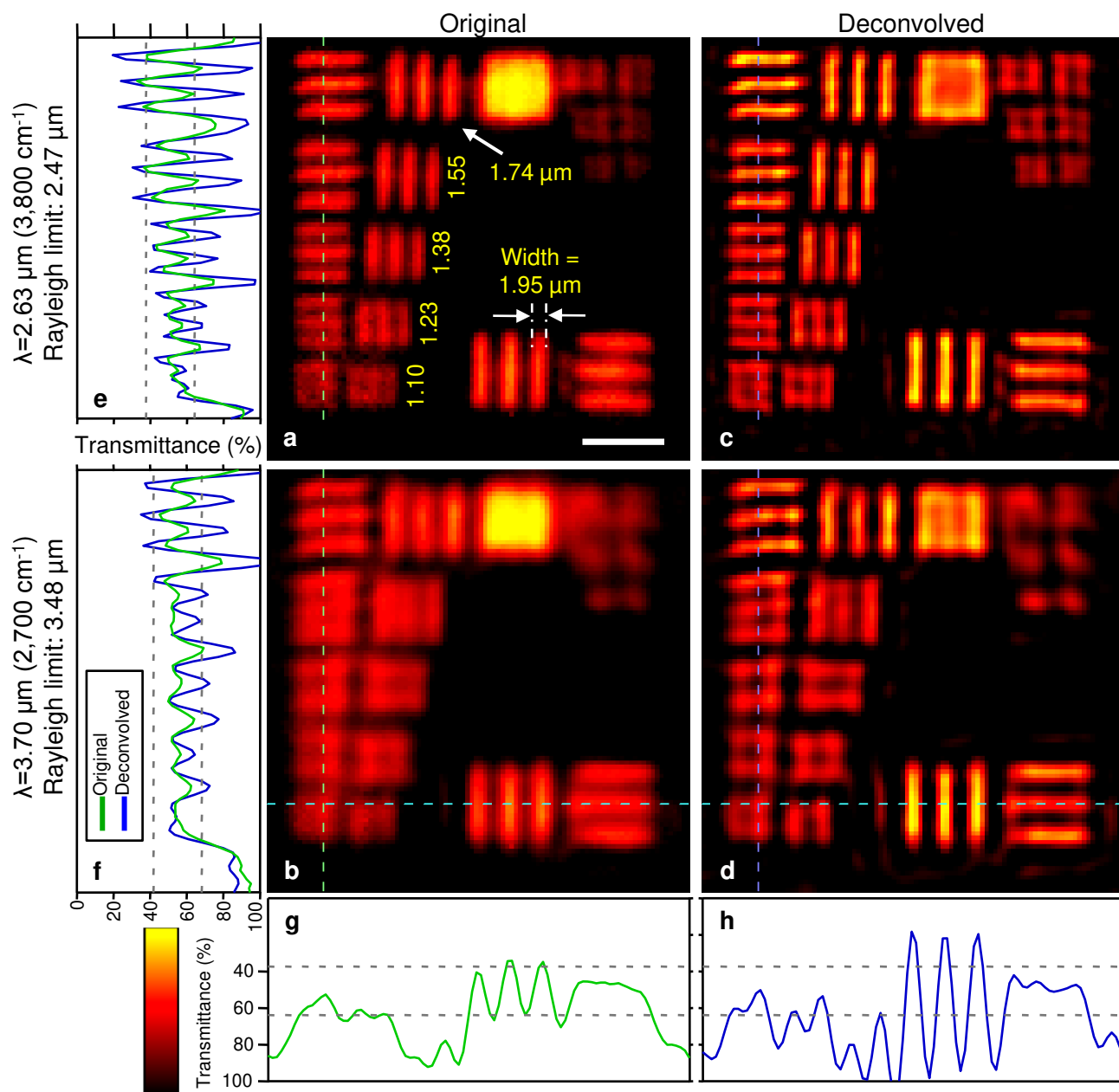
Supplementary Figure 1	Additional chemical images from various FTIR systems.
Supplementary Figure 2	Comparison of thermal and synchrotron source at high magnification.
Supplementary Figure 3	Transmission images of a high-resolution 1951 USAF test target.
Supplementary Figure 4	Reflection images of a high-resolution 1951 USAF test target.
Supplementary Figure 5	Point-spread-function (PSF) measurements and influence of pixel size.
Supplementary Figure 6	Wavenumber-dependent point-spread-function (PSF) measurements using sub-diffraction pinholes.
Supplementary Figure 7	FTIR Images of small, sub-diffraction sized polystyrene beads.
Supplementary Table 1	Comparison of some key quantities of various source-FTIR systems.
Supplementary Note 1	Infrared sources, detectors and coupling efficiencies
Supplementary Note 2	Spatial resolution
Supplementary Note 3	Infrared image deconvolution



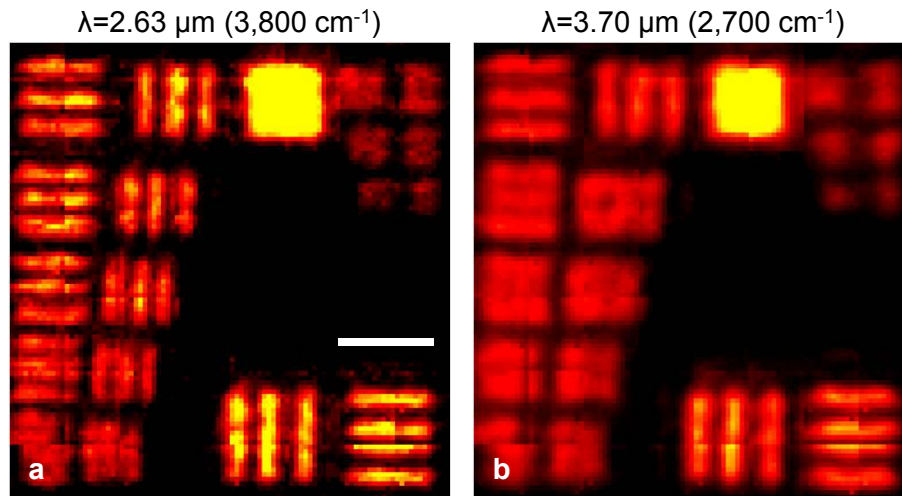
Supplementary Figure 1 | Additional chemical images from various FTIR systems. Panels **a–d** show the same unstained cancerous prostate tissue section as in **Figure 2**, but here using the peak height at $3,300\text{ cm}^{-1}$ (Amide A band, N-H stretch). **(a)** Attenuated total reflection (ATR) image acquired with a PerkinElmer Spotlight FTIR system using a ZnSe crystal ($1.56 \times 1.56\ \mu\text{m}^2$ pixel size). Even though ATR can provide relatively high spatial resolution, it is not really a far-field technique and requires close, homogeneous contact of a crystal with the sample surface. This requirement restricts the number of samples that can be studied with ATR and can potentially lead to sample damage and artifacts, for example due to sample parts sticking to the crystal and being dragged along during the acquisition (e.g., see the “line” in the lower left part of the image **a**, indicated by the green arrow). **(b)** A dual-aperture microscope (Thermo Nicolet Continuum) with a conventional single-beam synchrotron source. Such a setup can in principle yield diffraction-limited resolution at all wavelengths, but the small aperture ($3 \times 3\ \mu\text{m}^2$) and step size ($0.8\ \mu\text{m}$) required to achieve this make it practically impossible. For this sample, in particular, $\sim 135,000$ pixels would need to be mapped, which at $\sim 7\text{ s}$ (16 scans) per spectrum would require 11 days of uninterrupted mapping. Thus, sample size and acquisition time (here ~ 5 hours) can make larger apertures and step sizes necessary (here $10 \times 10\ \mu\text{m}^2$), leading to loss of resolution. In sharp contrast, we recorded the fully diffraction-limited image using the system presented here **(d)** with $\sim 295,000$ pixels in ~ 30 minutes (16 scans). **(c)** A thermal-source-equipped system (Bruker Hyperion 3000 using a 64×64 pixel FPA) with pixel size $0.54 \times 0.54\ \mu\text{m}^2$ loses spectral (see **e**) and image quality, making the approach impractical. **(d)** The multi-beam synchrotron image (pixel size $0.54 \times 0.54\ \mu\text{m}^2$) demonstrates far-field/contactless high spatial resolution and high spectral quality (see **e**). Both **c** and **d** have been acquired on the same instrument with identical imaging conditions. The crosshairs in **a–d** indicate the positions of the corresponding, unprocessed spectra (NH/OH and CH stretch region) shown in panel **e**. Yellow scale bar in **a**: $100\ \mu\text{m}$.



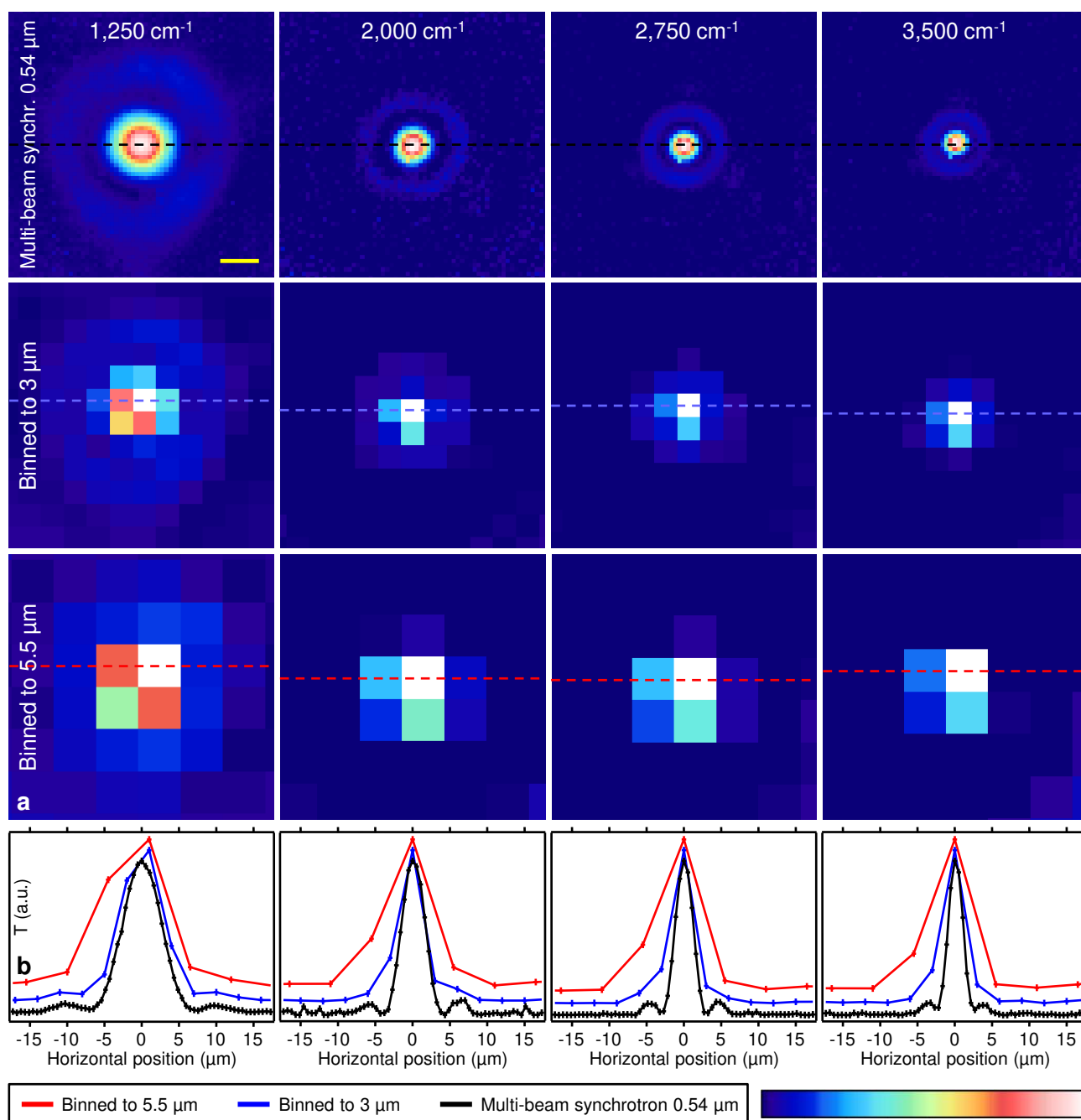
Supplementary Figure 2 | Comparison of thermal and synchrotron source at high magnification. **(a,b)** FPA images at $2,850\text{ cm}^{-1}$ (96×96 pixels, 32 scans, $74\times$ objective, pixel size $0.54 \times 0.54\ \mu\text{m}^2$) without sample using a thermal source **(a)** and the 12 overlapping synchrotron beams of the new system **(b)**. Both infrared images have been acquired with the same system (Bruker Hyperion 3000) under identical conditions and scaled the same to visually illustrate the spatial noise distribution over the entire FPA in both cases. The crosshairs in **a** and **b** indicate the positions of the single pixel 100% lines shown in **c** and **d**. The latter demonstrate an rms noise enhancement of 14.5 of the new versus the thermal system (calculated for $2,450\text{--}2,550\text{ cm}^{-1}$).



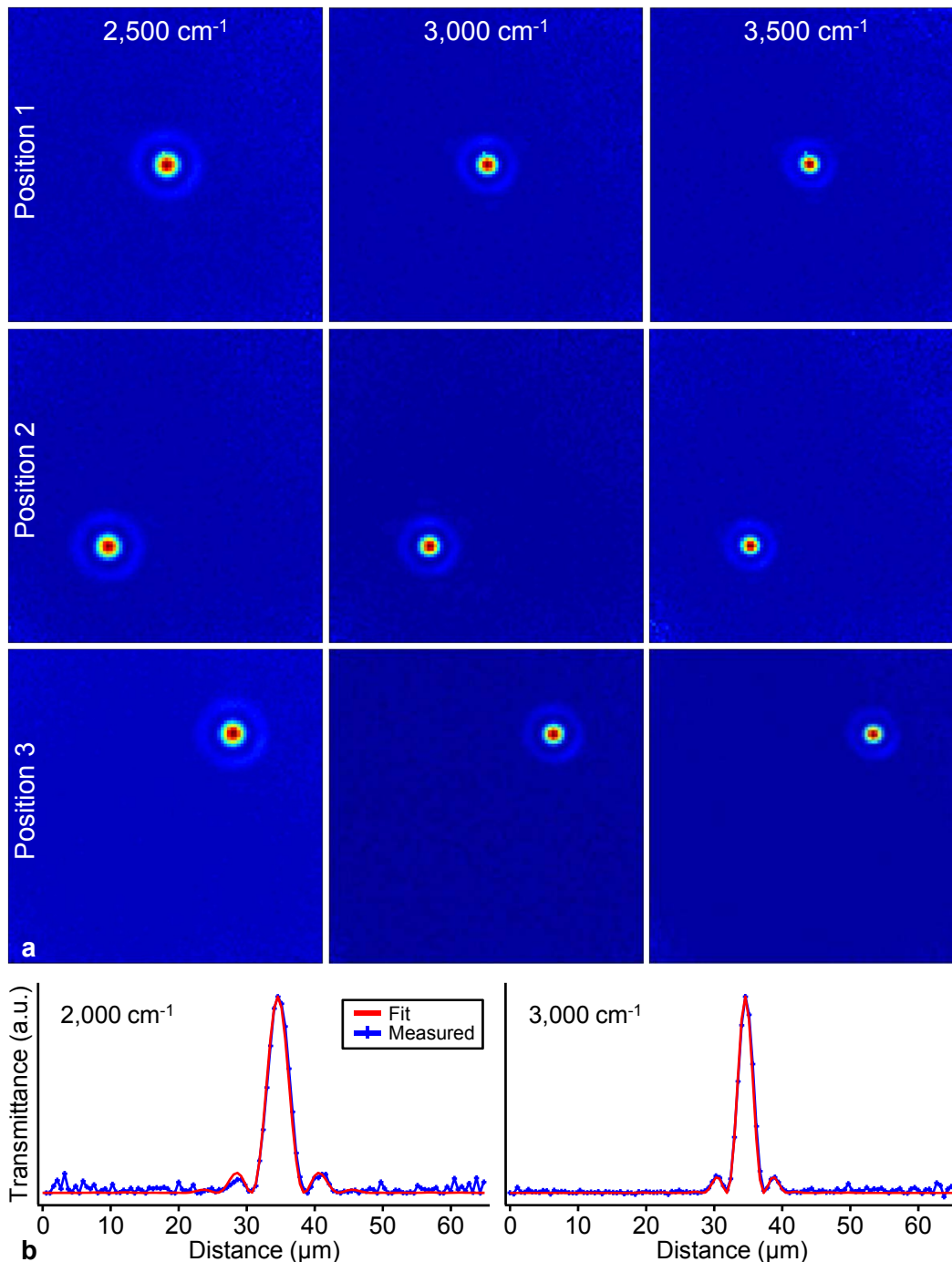
Supplementary Figure 3 | Transmission images of a high-resolution 1951 USAF test target. The target consists of chrome patterns on glass, which is infrared transparent above $\sim 2,200\text{ cm}^{-1}$. Groups 8 and 9 are shown (256–645 cycles / mm). (**a,b**) Unprocessed images in transmittance (96×96 pixels, 32 scans, pixel size $0.54 \times 0.54\ \mu\text{m}^2$, inverted color scale) at a wavelength of $2.63\ \mu\text{m}$ ($3,800\text{ cm}^{-1}$) and $3.70\ \mu\text{m}$ ($2,700\text{ cm}^{-1}$), respectively. Line profiles along the dashed lines in **a–d** are shown in **e–h**. The dashed gray lines in **e–h** delineate a contrast range of 26.4% corresponding to the Rayleigh resolution limit. White scale bar in **a**: $10\ \mu\text{m}$. This imaging system exceeds (see **Supplementary Note 2**) the theoretical Rayleigh resolution ($2.47\ \mu\text{m}$ for **a** and $3.48\ \mu\text{m}$ for **b**), since it can clearly resolve both the $1.74\ \mu\text{m}$ pattern (contrast 30.7%) and almost resolve the $1.55\ \mu\text{m}$ pattern (23.8%) in **a**, and resolve the $1.95\ \mu\text{m}$ pattern (29.1%) in **b**. Spatial oversampling (pixel size: $0.54 \times 0.54\ \mu\text{m}^2$) is a prerequisite for deconvolution techniques. Panels **c** and **d** show patterns **a** and **b** deconvolved with measurement-based point-spread-functions (see text). The resolution improvement is clearly visible in the images and in the line profiles: the contrast of the patterns with a width of $1.38\ \mu\text{m}$ and $1.74\ \mu\text{m}$ increase from 14.1% (unresolved) in **a** to 30.9% (resolved) in **c**, and from 13.7% (unresolved) in **b** to 40.2% (resolved) in **d**, respectively.



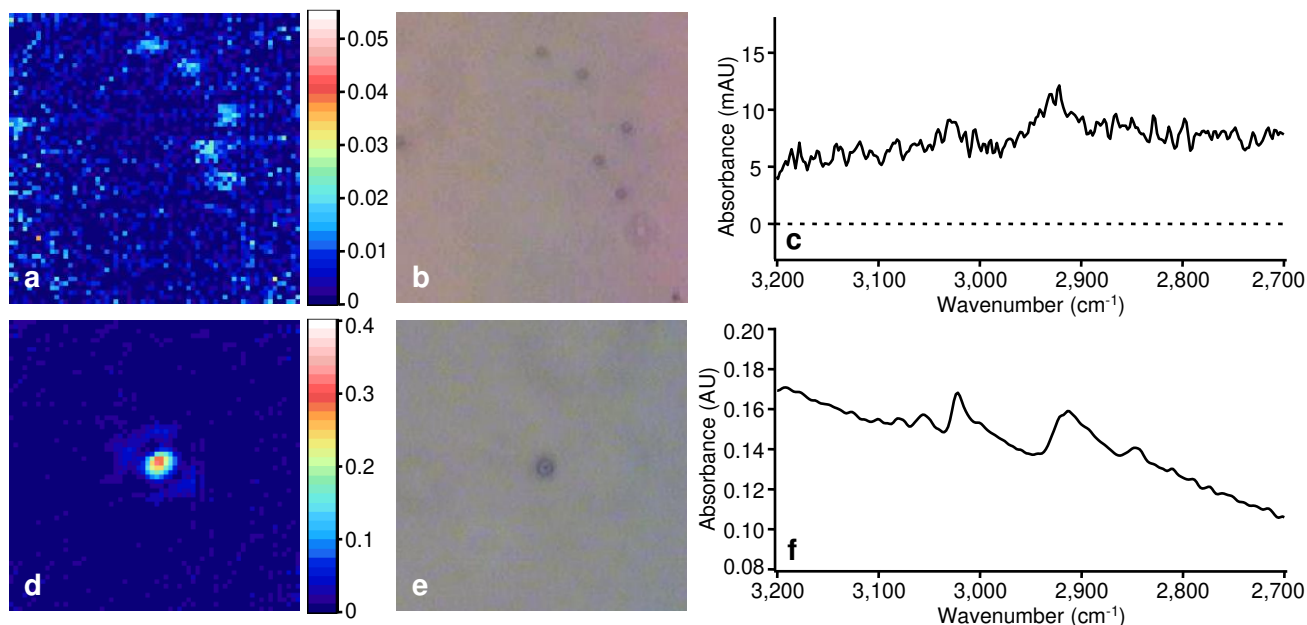
Supplementary Figure 4 | Reflection images of a high-resolution 1951 USAF test target. The same groups 8 and 9 as in **Supplementary Figure 3** are shown, here acquired in reflection mode. **(a,b)** Images (96 × 96 pixels, 8 × 6 tiles with 12 × 16 pixels/tile, 64 scans, pixel size 0.54 × 0.54 μm²) integrated around a wavelength of 2.63 μm (3,800 cm⁻¹) and 3.70 μm (2,700 cm⁻¹), respectively. White scale bar in **a**: 10 μm. Similar spatial resolution as in transmission mode (**Supplementary Fig. 3**) is achieved.



Supplementary Figure 5 | Point-spread-function (PSF) measurements and influence of pixel size. Measured transmittance (T) images (96×96 pixels, pixel size $0.54 \times 0.54 \mu\text{m}^2$) of pinholes with a diameter of $5 \mu\text{m}$ at $1,250 \text{ cm}^{-1}$ (wavelength $\lambda = 8 \mu\text{m}$, 200 scans) and with a diameter of $2 \mu\text{m}$ at $2,000$, $2,750$, and $3,500 \text{ cm}^{-1}$ ($\lambda = 5$, 3.6 , $2.9 \mu\text{m}$, 400 scans) are shown in the top row of panel **a** (yellow scale bar: $5 \mu\text{m}$). These pinholes can be considered sub-diffraction sized point sources for the given wavelengths. The first order diffraction ring is clearly resolved in each case. Post-acquisition binning to obtain a pixel size of 3×3 and $5.5 \times 5.5 \mu\text{m}^2$ (middle and bottom row in **a**) simulates the smallest reported pixel size for synchrotron-based mapping and commercial imaging instruments, respectively. These images, together with the corresponding line profiles (stacked) through the centers of the PSFs shown in **b** (positions indicated by the dashed lines in **a**), illustrate the impact of pixel size on achievable spatial resolution. Apart from the $3 \times 3 \mu\text{m}$ case at $1,250 \text{ cm}^{-1}$, none of the binned images reproduces the first minimum between the central maximum and the first order diffraction ring, which makes these images unusable as PSFs.



Supplementary Figure 6 | Wavenumber-dependent point-spread-function (PSF) measurements using sub-diffraction pinholes. **(a)** Multi-beam synchrotron transmittance images (96×96 pixels, 400 scans, pixel size $0.54 \times 0.54 \mu\text{m}^2$) of pinholes with a diameter of $2 \mu\text{m}$ at 2,500, 3,000, and 3,500 cm^{-1} at three different positions in the field of view. This pinhole corresponds to a sub-diffraction sized point source for all mid-infrared wavelengths and has been used as a PSF measurement. The first order diffraction ring (more pronounced for a Schwarzschild objective due to the central obscuration) and its size dependence on the wavenumber are clearly visible. It can also be seen that the PSF is nearly identical at various positions on the FPA confirming that the PSF can be assumed to be translationally invariant. **(b)** Two line profiles through the center of the measured pinhole image, as well as the corresponding fits of the theoretical model of a Schwarzschild objective to the measured curves for 2,000 and 3,000 cm^{-1} . The noise-free PSFs obtained from the fit to the measurements have been used for the image deconvolution shown in **Supplementary Figure 3c,d**.



Supplementary Figure 7 | FTIR Images of small, sub-diffraction sized polystyrene beads. **(a)** FTIR image of several polystyrene beads with a diameter of $1.025 \pm 0.07 \mu\text{m}$ (64×64 pixels, 256 scans, pixel size $0.54 \times 0.54 \mu\text{m}^2$, acquisition time ~ 6 min.) integrated over the CH_2 peak around $2,920 \text{ cm}^{-1}$. **(b)** Corresponding visible light image indicating the positions of the beads. **(c)** Typical unprocessed single-pixel spectrum from one of the polystyrene beads. The CH_2 peak has a signal-to-noise ratio (SNR) of around 3. These beads, which have a volume of 0.6 ± 0.1 femtoliter, a mass of 600 ± 100 femtogram and contain 6 ± 1 femtomole or $(3.4 \pm 0.7) \times 10^9$ CH_2 functional groups are at the detection limit for these imaging conditions. Spatial undersampling, more scans, or utilization of noise reduction algorithms may be used to further push the detection limit to smaller quantities. **(d–f)** Analogue data for one $2.061 \pm 0.024 \mu\text{m}$ diameter bead (200 scans, acquisition time ~ 4 min., other parameters identical). Here the SNR is ~ 7 – 9 . Panel **d** shows that this size bead (volume: 4.6 ± 0.2 femtoliter, mass: 4.8 ± 0.2 picogram, 46 ± 2 femtomole or $(2.8 \pm 0.1) \times 10^{10}$ CH_2 functional groups) can be imaged with reasonable quality, even showing the first order diffraction ring. These results demonstrate that the new system is very sensitive.

Sources:	Étendue	Photon flux	Brightness	Microscope / detection optics	Acceptance
Thermal	5.0×10^{-7}	9.0×10^{13}	1.8×10^{20}	Single element	2.0×10^{-10}
Synchrotron single beam	9.0×10^{-11}	7.8×10^{12}	8.7×10^{22}	FPA wide-field	4.5×10^{-9}
Multi-beam Synchrotron (this manuscript)	1.2×10^{-9}	1.0×10^{14}	8.3×10^{22}		

	Single element system		FPA wide-field system	
	Coupling efficiency	Photons on detector	Coupling efficiency	Photons on detector
Thermal	0.040	3.6×10^{10}	0.90	8.1×10^{11}
Synchrotron single beam	100	7.8×10^{12}	100	7.8×10^{12}
Multi-beam Synchrotron (this manuscript)	N/A	N/A	100	1.0×10^{14}

Supplementary Table 1 | Comparison of some key quantities of various source–FTIR systems. These numbers are based on the Synchrotron Radiation Center light source (average beam current $I = 200$ mA), Bruker Vertex 70 and Hyperion 3000 spectrometer and microscope both for the thermal source (at 1,300 K, $\lambda = 4$ μm , aperture diameter 2 mm) and the multi-beam system developed here using $NA = 0.6$, and 96×96 pixel FPA. The synchrotron single beam (extracting 25×25 mrad²) and single element detector is based on a Thermo Nicolet Continuum microscope with a $NA = 0.65$ objective using a 10×10 μm^2 aperture. Units: étendue/acceptance: $\text{m}^2 \text{rad}^2$, photon flux: photons / (s 0.1% bandwidth), brightness (radiance): photons / (s 0.1% bandwidth $\text{m}^2 \text{rad}^2$), coupling efficiency: %, photons on detector: photons / (s 0.1% bandwidth).

Supplementary Note 1

Infrared sources, detectors and coupling efficiencies

One disadvantage of conventional thermal mid-infrared sources is that they have a relatively low photon flux: compared to incandescent lamps in the visible they emit roughly 10 times less photons in the respective bandwidth (typically: 3,200 K for a tungsten-halogen lamp and 1,300 K for a mid-infrared glower). Their main drawback, however, is their large étendue or area–angle product, which dictates how efficiently optical components can be coupled. For a given flux, an efficient system conserves étendue whereas an étendue decrease necessarily involves photon loss and therefore ultimately impacts the instrumental SNR¹. Étendue (related to the emittance ε : $\varepsilon_x \times \varepsilon_y = \text{source étendue}$) is a very useful quantity because, together with the acceptance (= detection étendue) of the microscope/detection optics, it allows the calculation of the coupling efficiency^{1,2}. The coupling efficiency, defined as the ratio of the detection optics acceptance and the source étendue, describes how efficiently the light from the source can be collected and transmitted through the optical train to the detector (neglecting photon loss due to mirror reflectivities < 100%, etc.). The large étendue of a thermal source as compared to that of the microscope leads to a very low coupling efficiency and thus eventually to a much lower photon flux reaching the detector (estimated as source flux times coupling efficiency). A single synchrotron beam has lower flux than a thermal source but due to its high coupling efficiency it provides much higher flux to the detector. Ultimately, the flux at the detector determines the attainable spectral SNR per acquisition time³. **Supplementary Table 1** summarizes these key numbers for various instrumental configurations. The étendue also explains why, hypothetically postulating, coupling several thermal sources to obtain higher flux on the detector instead of using a low étendue, high brightness source would not lead to equivalent data. The étendue would increase with the number of thermal sources used, leading to a lower coupling efficiency. The low étendue of the synchrotron light, hence, is critical to achieving high SNR.

In contrast, lasers have a very small étendue leading to high coupling efficiencies. Nonetheless, laser-based infrared sources like lead salt diodes, optical parametric oscillators, difference frequency lasers etc. have a relatively narrow linewidth and tunability, which makes it difficult to cover the comparatively broad infrared bandwidth. Therefore they are mostly used in narrow-bandwidth, high-sensitivity measurements. Examples include trace species in gas streams⁴. Much more recently the development of quantum cascade lasers (QCLs) has made tremendous progress⁵ and they have become the laser of choice for a major part of the infrared spectrum. In contrast to conventional lasers, whose emission wavelength is based on interband transition energies—an intrinsic material property—, QCLs' center wavelength of operation is determined by the material layer thickness. The latter can thus be chosen freely within a fairly wide range⁵ of $\sim 530\text{--}2,860\text{ cm}^{-1}$; however this bandwidth to date has only been demonstrated in prototypes. They currently cannot access important parts of the mid-infrared spectrum, such as the CH-stretch region from $\sim 2,860\text{--}3,100\text{ cm}^{-1}$ and the OH/NH region around $3,400\text{ cm}^{-1}$. Furthermore, even though they offer relatively high tunability around their center wavenumber (up to $\sim 200\text{ cm}^{-1}$ continuous wave and $\sim 300\text{ cm}^{-1}$ pulsed⁵, in prototypes), half a dozen or more QCLs have to be combined to obtain gapless tunability over a broad bandwidth. Synchrotron storage rings, in contrast, are a bright, stable and broadband light source.

Supplementary Note 1 References

1. Duerst, R.W. et al. IR Spectral Optimization. *Practical Guide to Infrared Microspectroscopy* **19**, 145-151 (1995).
2. Duncan, W.D. & Williams, G.P. Infrared synchrotron radiation from electron storage rings. *Appl. Opt.* **22**, 2914-2923 (1983).
3. May, T.E., Bosch, R.A. & Julian, R.L. Infrared Edge Radiation Beamline At Aladdin. *Proceedings of the 1999 Particle Accelerator Conference* 2394-2396 (1999).
4. Sigrist, M. et al. Trace gas monitoring with infrared laser-based detection schemes. *Appl. Phys. B* **90**, 289-300 (2008).
5. Curl, R.F. et al. Quantum cascade lasers in chemical physics. *Chem. Phys. Lett.* **487**, 1-18 (2010).

Supplementary Note 2

Spatial resolution

Supplementary Figure 3 in the main text confirms that the infrared imaging system presented here not only reaches the Rayleigh resolution criterion, but actually exceeds it considerably. **Supplementary Figure 3a**, for example, shows the image of the USAF pattern at 2.63 μm wavelength for which the Rayleigh limit is 2.47 μm . The corresponding line profile in **Supplementary Figure 3e**, however, confirms that we can resolve the pattern with a width of 1.74 μm (it really is the bar *width* that is relevant here, see references ^{1,2}). Similarly, in **Supplementary Figure 3b** we can resolve the 1.95 μm pattern, even though the Rayleigh limit is 3.48 μm in this case. We believe that one factor that contributes to that effect is the use of Schwarzschild objectives, which have a central obscuration due to the convex mirror. This leads not only to an increase in the higher order maxima intensity, but also in slight shifts of the side minima and maxima of the diffraction pattern. This in turn modifies the Rayleigh criterion equation, which is defined as the distance from the central maximum to the first side minimum. From the fit routines we used to obtain the calculated, noise-free point-spread-functions (PSFs) we estimate the usual prefactor in the usual Rayleigh equation to be ~ 0.5 instead of the usual 0.61. It is interesting to note that reference ¹ also observed a resolution better than expected with the same Bruker instrument, but using a thermal source and a different objective.

Other techniques promising high or even sub-diffraction spatial resolution are attenuated total reflection (ATR) imaging³ (**Supplementary Fig. 1a**) or near-field methods^{4,5}, but they require close contact of a crystal or probe with the sample, have a limited sampling volume and have the potential to alter or damage the sample under investigation. Furthermore, near-field approaches are rather complex instrumentally, provide low SNR, which makes covering large samples time-consuming, and are not readily accessible.

Supplementary Note 2 References

1. Lasch, P. & Naumann, D. Spatial resolution in infrared microspectroscopic imaging of tissues. *Biochim. Biophys. Acta - Biomembranes* **1758**, 814-829 (2006).
2. Themelis, G., Yoo, J.S., Soh, K., Schulz, R.B. & Ntziachristos, V. Real-time intraoperative fluorescence imaging system using light-absorption correction. *J. Biomed. Opt.* **14**, 064012 (2009).
3. Kazarian, S.G. & Chan, K.L.A. Micro- and Macro-Attenuated Total Reflection Fourier Transform Infrared Spectroscopic Imaging. *Appl. Spectrosc.* **64**, 135A-152A (2010).
4. Knoll, B. & Keilmann, F. Near-field probing of vibrational absorption for chemical microscopy. *Nature* **399**, 134-137 (1999).
5. Rice, J.H. Nanoscale optical imaging by atomic force infrared microscopy. *Nanoscale* **2**, 660-667 (2010).

Supplementary Note 3

Infrared image deconvolution

We implemented a Fourier-based deconvolution algorithm to deconvolve the point-spread-function (PSF) of the 74× objective from measured hyperspectral data. The algorithm utilized PSFs determined from measured infrared transmittance through a 2 μm pinhole (**Supplementary Figs. 5 and 6**) fitted to a model diffraction pattern of a Schwarzschild objective taking into account the central obscuration^{1,2}. Note that the high spatial resolution of our system permitted us to resolve the first order diffraction ring at each wavelength. The noise-free PSFs obtained from the fit reflect the actual experimental setup and have been used for the deconvolution process. The data was preprocessed by imposing reflexive boundary conditions; i.e., the boundaries of the data were assumed to consist of mirror images on either side of the boundary; in this way ringing artifacts at the image boundaries introduced from the discrete Fourier transform (FT) were avoided. The deconvolution process was performed by taking 2D Fast Fourier Transforms (FFTs) of the data and PSFs at each wavenumber over the entire mid-infrared spectral range. Subsequently, we divided the FTs of the images by the optical transfer function (OTF, = FT of the PSF) and applied a frequency-dependent Hanning filter to the resulting data to suppress enhanced noise. Finally, inverse FFTs (IFFTs) were performed on each 2D Fourier data set, resulting in deconvolved images at each wavenumber. The deconvolved images were rescaled by requiring that the total intensity in the image be conserved, and reassembled in a reconstructed hyperspectral cube.

The resulting data sets consisted of images with enhanced contrast and spatial resolution and spectra that have not been contaminated by diffracted light from neighboring regions. We tested the algorithm on several different test samples including polystyrene beads and tissue (data not shown), confirming that the spatially deconvolved reconstructed spectra preserve all the original spectral features and follow the unprocessed spectra relatively closely. This

demonstrates that the deconvolution and spectral reconstruction process does not introduce artifacts, for example from noise in the original images.

Supplementary Note 3 References

1. Carr, G.L. Resolution limits for infrared microspectroscopy explored with synchrotron radiation. *Rev. Sci. Instrum.* **72**, 1613-1619 (2001).
2. Carr, G.L., Chubar, O. & Dumas, P. Multichannel detection with a synchrotron light source: design and potential. *Spectrochemical Analysis Using Infrared Multichannel Detectors* 56-84 (2005).

observed no spectral evidence of spatial or temporal coherence effects, nor any impact on image quality or resolution, as can be seen, for example, by the correspondence between the thermal and synchrotron spectral data.

Experimental details, data processing, and samples. We conducted conventional thermal source-based imaging on two commercial systems: Stingray (Varian; **Fig. 2c**) using an FPA detector and Spotlight 400 (PerkinElmer; **Figs. 2a,b** and **3d,e** and **Supplementary Fig. 1a**) equipped with a single element and a 16-pixel linear array detector. We acquired the synchrotron point-by-point scanning image (**Supplementary Fig. 1b**) on a Continuum (Thermo Nicolet) dual-aperture microscope connected to beamline 031, and we collected the remaining images with the multibeam synchrotron system connected to a Hyperion 3000 (Bruker) microscope at beamline 021, both at the Synchrotron Radiation Center. The Varian, PerkinElmer and Thermo Nicolet measurements used a Happ-Genzel, the Bruker measurements a Norton-Beer (medium) apodization. We baseline-corrected the images in **Figures 2** and **3** (including spectra), **Supplementary Figures 1** and **7**; all other infrared images as well as spectra show raw data. We did not use post-acquisition smoothing or filtering. The infrared data were analyzed and images were created with software packages IRidys (in-house development) and ENVI (ITT VIS).

The prostate cancer sample (Gleason grade 6) with epithelial cells (**Fig. 2** and **Supplementary Fig. 1**) was a viable tumor without necrosis, in a cribriforming pattern and had some strands of stroma crossing through it. A second prostate cancer sample, which was also Gleason grade 6 for comparison (**Fig. 3a–e**), had chronic inflammation (mostly mononuclear cell infiltration of macrophages and lymphocytes) and contained two glands, a small vessel with a muscular wall and capillaries (with blood). The tissue shown in **Figure 3f** was a normal human breast tissue core including the terminal ductal lobular unit (TDLU) region and the tissue shown in **Figure 3h** contained two benign prostate glands from a cancerous prostate tissue core (Gleason grade 6). Tissues used here were from anonymized samples from individuals and involved secondary analysis as approved by the University of Illinois at Urbana-Champaign Institutional Review Board, protocol 06684. We fixed all biomedical samples in 4% paraformaldehyde, embedded them in paraffin, sectioned them at a thickness of 4 μm , mounted them on a BaF₂ infrared transparent window and deparaffinized them with hexane for 48 h before

measurement. In transmission mode sample thickness can affect the obtainable spatial resolution. Using a simple geometric model we estimated that the sample thickness should not be above $\sim 3\text{--}4$ μm to achieve full diffraction-limited resolution.

We purchased the apertures (**Supplementary Figs. 5** and **6**) from National Aperture, Inc., the high-resolution US Air Force (USAF) test target (**Supplementary Fig. 3**) from Edmund Optics Inc. and the polystyrene beads (**Supplementary Fig. 7**) from Polysciences, Inc. We diluted the polystyrene bead suspension with water, dispensed it on an ultrathin formvar film substrate and then air-dried it.

We recorded images of polystyrene beads with a diameter of ~ 1 and 2 μm (acquisition time, ~ 5 min) to examine spectral limits of detection per pixel. We detected the 6 ± 1 fmol or 3.4×10^9 ($\pm 0.7 \times 10^9$; s.d.) CH₂ groups contained in a 1 μm polystyrene bead (mass, 600 ± 100 fg; volume, 0.6 ± 0.1 fl) in a single $0.54 \mu\text{m} \times 0.54 \mu\text{m}$ pixel using the International Union of Pure and Applied Chemistry (IUPAC) detection limit criterion (**Supplementary Fig. 7**). We estimated this to be ~ 100 -fold better than with current instrumentation¹⁶ and this compared favorably with the lowest detection limit reported³⁵ using destructive methods.

- Li, Z.Q. *et al. Nat. Phys.* **4**, 532–535 (2008).
- Bunaciu, A.A., Aboul-Enein, H.Y. & Fleschin, S. *Appl. Spectrosc. Rev.* **45**, 206–219 (2010).
- Matveev, S. & Stachel, T. *Geochim. Cosmochim. Acta* **71**, 5528–5543 (2007).
- Prati, S., Joseph, E., Sciutto, G. & Mazzeo, R. *Acc. Chem. Res.* **43**, 792–801 (2010).
- Politi, Y., Arad, T., Klein, E., Weiner, S. & Addadi, L. *Science* **306**, 1161–1164 (2004).
- Martin, F.L. *et al. Nat. Protoc.* **5**, 1748–1760 (2010).
- Hazen, T.C. *et al. Science* **330**, 204–208 (2010).
- Walsh, M.J. *et al. Stem Cells* **26**, 108–118 (2008).
- Walsh, M.J. *et al. Stem Cell Res.* **3**, 15–27 (2009).
- Holman, H.N., Bechtel, H.A., Hao, Z. & Martin, M.C. *Anal. Chem.* **82**, 8757–8765 (2010).
- Kuzyk, A. *et al. J. Biol. Chem.* **285**, 31202–31207 (2010).
- Webster, G.T. *et al. Anal. Chem.* **81**, 2516–2524 (2009).
- Bhargava, R. *Anal. Bioanal. Chem.* **389**, 1155–1169 (2007).
- Centonze, V. & Pawley, J.B. in *Handbook of Biological Confocal Microscopy* 3rd edn. (ed. Pawley, J.B.) 627–649 (Springer, New York, 2006).
- Murphy, D.B. *Fundamentals of Light Microscopy and Electronic Imaging* 1st edn. 233–258 (Wiley-Liss, New York, 2001).
- Bobroff, N. *Rev. Sci. Instrum.* **57**, 1152–1157 (1986).
- Reffner, J.A., Martoglio, P.A. & Williams, G.P. *Rev. Sci. Instrum.* **66**, 1298–1302 (1995).
- Nasse, M.J., Reininger, R., Kubala, T., Janowski, S. & Hirschmugl, C. *Nucl. Instrum. Methods Phys. Res. A* **582**, 107–110 (2007).
- Park, K., Lee, J., Bhargava, R. & King, W.P. *Anal. Chem.* **80**, 3221–3228 (2008).